Published in final edited form as:
Comput Methods Biomech Biomed Engin. 2014 June ; 17(8): 838–844. doi: 10.1080/10255842.2012.719606.

Computational Analysis of Lung Deformation after Murine neumonectomy

Nenad Filipovic[1,2], **Barry C. Gibney**[3], **Dalibor Nikolic**[1], **Moritz A. Konerding**[4], **Steven J. Mentzer**[3], and **Akira Tsuda**[2]

Nenad Filipovic: nfilipov@hsph.harvard.edu; Barry C. Gibney: bgibney@partners.org; Dalibor Nikolic: markovac85@kg.ac.rs; Moritz A. Konerding: konerdin@uni-mainz.de; Akira Tsuda: atsuda@hsph.harvard.edu

[1]Faculty of Mechanical Engineering, University of Kragujevac, Serbia

[2]Molecular and Integrative Physiological Sciences, Harvard School of Public Health, Boston, MA

[3]Laboratory of Adaptive and Regenerative Biology, Brigham & Women's Hospital, Harvard Medical School, Boston MA

[4]Institute of Functional and Clinical Anatomy, University Medical Center of Johannes Gutenberg-University, Mainz, Germany

Abstract

In many mammalian species, the removal of one lung (pneumonectomy) is associated with the compensatory growth of the remaining lung. To investigate the hypothesis that parenchymal deformation may trigger lung regeneration, we used microCT scanning to create 3-dimensional finite element geometric models of the murine lung pre- and post-pneumonectomy (24 hours). The structural correspondence between models was established using anatomic landmarks and an iterative computational algorithm. When compared with the pre-pneumonectomy lung, the post-pneumonectomy models demonstrated significant translation and rotation of the cardiac lobe into the post-pneumonectomy pleural space. 2-dimensional maps of lung deformation demonstrated significant heterogeneity ; the areas of greatest deformation were present in the subpleural regions of the lobe. Consistent with previously identified growth patterns, subpleural regions of enhanced deformation are compatible with a mechanical signal—likely involving parenchymal stretch—triggering lung growth.

Keywords

finite element; lung; image registration; regeneration; pneumonectomy

1. Introduction

The shape of the lung, reflecting the elastic properties of alveolar septae and transpleural pressures, is relevant to both normal respiratory function and lung regeneration. During normal tidal breathing, the lung demonstrates relative shape stability and geometric similarity (Miki *et al.*, 1993); that is, the shape of the lung remains relatively constant despite a change in lung volume. Computational modeling during normal breathing has largely focused on the mapping of lung motion relevant to the targeting of radiation therapy for lung tumors (Al-Mayah *et al.*, 2008, Werner *et al.*, 2009).

Correspondence: Dr. Steven J. Mentzer, Room 259, Brigham & Women's Hospital, 75 Francis Street, Boston, MA 02115, smentzer@partners.org; Tel: 617-732-6703; Fax: 617-249-0821.

In contrast, there is a fundamental change in the shape of the lung—independent of tidal ventilation—after the surgical removal of lung tissue. In rodents, microCT imaging after the removal of the left lung (pneumonectomy) has suggested a significant change in the shape of the remaining right lung (Gibney *et al.*, 2012). Subsequent analyses of the remaining lung, and the cardiac lobe in particular, have demonstrated significant increases in volume, weight, and cell number (Chamoto *et al.*, 2012, Konerding *et al.*, 2012, Lin *et al.*, 2011). The shape instability of the post-pneumonectomy lung suggests a mechanical or stretch signal for compensatory growth; however, the deformational changes in the remaining lung after pneumonectomy are poorly understood.

In this report, we used pre- and post-pneumonectomy microCT scanning to create finite element models of the murine cardiac lobe. We characterized the deformation of the post-pneumonectomy lung with an iterative nonrigid spatial transformation. Our finite element models were used to map lobar deformation and predict regions of regenerative growth within the murine cardiac lobe.

2. Pneumonectomy and imaging

Mice

C57/B6 mice (Jackson Laboratory, Bar Harbor, Maine), 22 to 30gm, were used in all experiments. The care of the animals was consistent with guidelines of the American Association for Accreditation of Laboratory Animal Care (Bethesda, MD).

Orotracheal intubation and ventilation

Orotracheal intubation was performed with the animal suspended by the incisors and the tongue gently retracted anteriorly. A 20G angiocatheter (BD Insyte, Sandy, Utah) was passed between the vocal cords under direct illumination. Anesthesia for orotracheal intubation was a mixture of 100mg/kg Ketamine (Fort Dodge Animal Health) and 0.6mg/kg Xylazine (Phoenix Scientific, Inc., St. Joseph, MO) administered intraperitoneally. For subsequent CT imaging, the mouse was maintained on 0.5% isofluorane, a respiratory rate of 200 bpm and a tidal volume of 10 ml/kg.

Pneumonectomy

Mice were intubated with a 20g angiocatheter (BD Insyte, Sandy, UT) and ventilated with a Flexivent rodent ventilater (SCIREQ, Montreal, QC Canada) using standard settings of 200 bpm, 10 ml/kg, a pressure limit of 30 cmH_2O and a PEEP of 3 cmH_2O (Gibney *et al.*, 2011). A left thoracotomy was performed through the 5th intercostal space, the hilum ligated with a 6-0 silk tie (Ethicon, Somerville, NJ), and the lung sharply excised distal to the ligature. A recruitment maneuver was performed to recruit the contralateral lung and medialize the mediastinum as the thoracotomy was closed. The mouse was extubated and transferred to a warmed cage until recovered from the anesthesia.

CT scans

CT scans alone were obtained with a GE eXplore 120 CT scanner at 50um/pixel resolution. The serial DICOM images were exported for use in custom finite element software previously described (Kojic *et al.*, 2008, Milasinovic *et al.*, 2008).

3. Numerical Method

Geometric model

We used a detailed image algorithm based on the 3D image reconstruction of the cardiac lobe both pre- and post-pneumonectomy. The 3D image model was created by combining the sequential 2D segmented images into one matrix image file. Using the matrix file, the boundary surface of the 3D mesh was constructed based on the marching cubes algorithm (Milasinovic *et al.*, 2008). The surface was idealized using a standard Laplacian smoothing algorithm and surface cleaning. Using a connectivity analysis previously described (Tsuda *et al.*, 2008), the cardiac lobe was isolated from the rest of the lung. The resulting geometric models, typically about 81,000 3D 8-node finite elements using unstructured discretization, provided a faithful reproduction of the cardiac lobe observed in vivo. The central axis of the cardiac lobe airway, branching from the right mainstem bronchus, was used as a reference point for translation and a reference axis for rotation calculations.

Spatial correspondence of pre- and post-pnemonectomy lung

The registration of pre- and post-pneumonectomy lung images was approached using a nonrigid spatial transformation. The number of surface finite elements in the post-pneumonectomy geometric model (Figure 2i, red mesh) was larger than in the pre-pneumonectomy model (Figure 2i, blue mesh). The spatial correspondence was established with the following iterative steps:

Step 1: *Define the "key" connections between the corresponding nodes in the pre- and post-pneumonectomy geometric models*. Manually selected based on anatomic landmarks, the key nodes (Figure 2i, red arrows) provided structural correspondence that was interpolated by the subsequent automated steps of the algorithm. The number of key nodes, particularly relevant for concave surfaces, directly contributed to mapping accuracy and the increased number of elements in the post-pneumonectomy analysis.

Step 2: *Define nodes neighboring the landmark or "key" nodes*. For the nodes neighboring the key node (Figure 2ii, B, C, D), the algorithm automatically identified the corresponding node (B', C', D') in the post-pneumonectomy mesh by the following search process:

a. Assign a vector $\vec{a}$ (= AA') to each non-key node of the pre-pneumonectomy mesh. The vector $\vec{a}$ functions as a direction vector (Figure. 2 *ii* inset).

b. Evaluate connections between the node under consideration (e.g. node B) and the neighboring nodes in the post-pneumonectomy mesh (e.g. the node B', C', or D').

c. Identify the vector (among BB', BC', or BD') defining the smallest angle with $\vec{a}$; this vector provides a tentative identification of the corresponding node (e.g. node B') in the post-pneumonectomy mesh. BB' and is referred to as a temporary connection (Figure 2*ii*, blue arrows).

d. Exclude elements on the surface of the mesh by restricting the angle between $\vec{b_1}$ and $\vec{b_2}$ to less than 90 degrees (Figure 2*iii*, middle); an angle greater than 90 degrees identifies a surface with an opposite orientation (Figure 2*iii*, left).

For the case of a node (e.g. R) with two or more key nodes in their neighborhood (Figure 2*iv*),

e. Calculate the sum of the vectors of the nearest "key" connections, $\vec{a_1}$(= A_1A_1') and $\vec{a_2}$(= A_2A_2'), and assign the resulting $\vec{r}$ (= $\vec{a_1}$ + $\vec{a_2}$) to the node R as a direction vector (Figure 2*iv*).

f. Repeat (c) using $\vec{r}$ instead of $\vec{a}$, to identify a temporary connection.

g. Repeat (d) to ensure the proper orientation of surface element.

Step 3: *Check the validity of the newly formed temporary connections*. Test whether the newly identified corresponding node R' is located within an existing element created in the previous iterations (Figure 2*v*). After satisfying the required conditions, the connection RR' is considered "permanent". It will be used as a "key" connection in the next iteration (Figure 2*vi*).

Step 4: The iteration is repeated until all connections are assigned to all nodes in the pre-pneumonectomy mesh (Figure 2*vii*).

Deformation

The microCT imaging experiments demonstrated a substantial change in the shape of the cardiac lobe in the pre- pneumonectomy (undeformed configuration) and in the post-pneumonectomy (deformed configuration). Because the deformation of the remaning lung was not infinitesimal, we applied large deformation theory (Malvern, 1969); that is, the differential vector, $d\boldsymbol{x}$ in the post-pneumonectomy object was mapped from the original differential vector $d\boldsymbol{X}$ in the pre- pneumonectomy using the deformation gradient tensor $\tilde{\boldsymbol{D}}$

$$d\boldsymbol{x}=\tilde{D}d\boldsymbol{X} \quad (1)$$

where $d\boldsymbol{x}=\begin{bmatrix} x \\ y \\ z \end{bmatrix}$, $d\boldsymbol{X}=\begin{bmatrix} X \\ Y \\ Z \end{bmatrix}$, and $\tilde{\boldsymbol{D}}=\begin{bmatrix} \frac{\partial x}{\partial X} & \frac{\partial x}{\partial Y} & \frac{\partial x}{\partial Z} \\ \frac{\partial y}{\partial X} & \frac{\partial y}{\partial Y} & \frac{\partial y}{\partial Z} \\ \frac{\partial z}{\partial X} & \frac{\partial z}{\partial Y} & \frac{\partial z}{\partial Z} \end{bmatrix}$

Since the deformation gradient tensor $\tilde{\boldsymbol{D}}$ can be decomposed into a product of the rotation tensor $\tilde{\boldsymbol{R}}$ and the stretch tensor $\tilde{\boldsymbol{S}}$ using the polar decomposition theorem (Eringen, 1962), the total deformation (i.e., a product of rotation and stretch) can be expressed by $\tilde{\boldsymbol{D}}$. Total deformation was expressed as the "relative deformatin index" (RDI); a dimensionless measure reflecting the product of stretch and rotation.

Finite element procedure

In general, the finite element equation of balance of linear momentum can be derived from the fundamental differential equations of balance of forces acting at an elementary material volume. By applying the principle of virtual work, the differential equations of motion of a finite element are obtained as

$$\tilde{\boldsymbol{M}}\ddot{\boldsymbol{U}}+\tilde{\boldsymbol{B}}^{w}\dot{\boldsymbol{U}}+\tilde{\boldsymbol{K}}\boldsymbol{U}=\boldsymbol{F}^{ext} \quad (2)$$

where $\tilde{\boldsymbol{M}}$ is the mass matrix; $\tilde{\boldsymbol{B}}^{W}$ is the damping matrix; $\tilde{\boldsymbol{K}}$ is the stiffness matrix; and $\boldsymbol{U}$ and $\boldsymbol{F}^{ext}$ are the nodal displacement and the external nodal force vector which includes body and surface forces acting on the element, respectively. In the present analysis, we excluded intertial and viscous terms. Differential equations further integrated according to equation are:

$$\tilde{\boldsymbol{K}}_{tissue}{}^{n+1}\boldsymbol{U}={}^{n+1}\hat{\boldsymbol{F}} \quad (3)$$

where the tissue stiffness matrix $\tilde{\boldsymbol{K}}_{tissue}$ and vector ${}^{n+1}\boldsymbol{F}$ were expressed in terms of the matrices and vector described previously (Hoffmann & Rossignac, 1996). Notably, this equation reflected the assumptions of a linear elastic material and small displacement.

In the case of post-pneumonectomy shape change, the large wall displacements created a geometrically nonlinear, but materially linear problem. Because of the uncertain assumptions of equation (3), we used the previously described incremental-iterative equation (Kojic *et al.*, 2008):

$$ {}^{n+1}\tilde{\boldsymbol{K}}_{tissue}^{(i-1)}\boldsymbol{\Delta U}^{(i)} = {}^{n+1}\boldsymbol{F}^{(i-1)} - {}^{n+1}\boldsymbol{F}^{\mathrm{int}(i-1)} \quad (4) $$

where $\boldsymbol{\Delta U}^{(i)}$ were the nodal displacement increments for the iteration '*i*', and the system matrix ${}^{n+1}\tilde{\boldsymbol{K}}_{tissue}^{i-1}$, the force vector ${}^{n+1}\boldsymbol{F}^{(i-1)}$ and the vector of internal forces ${}^{n+1}\boldsymbol{F}^{\mathrm{int}(i-1)}$ correspond to the previous iteration. The geometrically linear part of the stiffness matrix, $\left(\tilde{\boldsymbol{K}}^{n+1}{}_{L}\right)_{tissue}^{(i-1)}$, and nodal force vector, ${}^{n+1}\boldsymbol{F}^{\mathrm{int}(i-1)}$, were defined in equation:

$$ \left({}^{n+1}\tilde{\boldsymbol{K}}_{L}\right)_{tissue}^{(i-1)} = \int_{V} \tilde{\boldsymbol{B}}_{L}^{T}{}^{n+1}\tilde{\boldsymbol{C}}_{tissue}^{(i-1)}\tilde{\boldsymbol{B}}_{L}\,dV, \quad \left({}^{n+1}\boldsymbol{F}^{\mathrm{int}}\right)^{(i-1)} = \int_{V} \tilde{\boldsymbol{B}}_{L}^{T}{}^{n+1}\tilde{\boldsymbol{\sigma}}^{(i-1)}\,dV \quad (5) $$

where the consistent tangent constitutive matrix ${}^{n+1}\tilde{\boldsymbol{C}}_{tissue}^{i-1}$ of tissue and the stresses at the end of time step ${}^{n+1}\tilde{\boldsymbol{\sigma}}^{(i-1)}$ depended on the material model used. Calculation of the matrix ${}^{n+1}\tilde{\boldsymbol{C}}_{tissue}^{i-1}$ and the stresses ${}^{n+1}\tilde{\boldsymbol{\sigma}}^{(i-1)}$ for the tissue material models used in these applications.

4. Results

The 3D geometric models were constructed with a greater number of surface elements in the post-pneumonectomy object (35,210 elements) than in the pre-pneumonectomy object (6348 elements) to ensure accurate feature correspondence in the post-pneumonectomy model. The average finite element model was composed of 81,100 3D 8-node elements. The models demonstrated important differences between the pre- and post-pneumonectomy lung (Figure 3). Most notably, there was significant displacement of the cardiac lobe into the left hemithorax (Figure 3B, ellipse). There was significant translation and rotation of the cardiac lobe into the post-pneumonectomy pleural space as well as displacement of the tip as the apparent result of contact with the chest wall. In addition, superimposition of the pre- and post-pneumonectomy mesh demonstrated a significant change in the shape of the cardiac lobe (Figure 3C). More than the other 3 lobes of the right lung, the cardiac lobe demonstrated the greatest displacement and shape change; perhaps not coincidently, the cardiac lobe also demonstrates the greatest increase in post-pneumonectomy lung growth (Gibney *et al.*, 2012).

To identify structural correspondence between the pre- and post-pneumonectomy cardiac lobes, 40 landmarks reflecting identifiable surface features were identified in both models (Figure 4). Referred to as "key" features, the key nodes provided an anchor for subsequent algorithmic mapping of the pre- and post-pneumonectomy surface elements. In comparing the models, an interesting finding was the discordance between the displacement and deformation of the cardiac lobe (Figure 5). Areas of the lung with the greatest displacement, such as the lateral tip of the cardiac lobe (illustrated in Figure 4), did not demonstrate significant deformation. In contrast, the posterior aspect of the cardiac lobe had minimal displacement, but significant deformation.

To provide a 2D map of parenchymal deformation, analogous to tissue sections obtained in standard histology, the finite element model of the cardiac lobe was serially sectioned in the transverse plane (Figure 6). The 2D maps of the cardiac lobe demonstrated that areas of greatest deformation were consistently present in the subpleural regions of the lobe. Subpleural regions of enhanced deformation and central regions of limited deformation,

were consistent with the growth patterns previously identified by microCT and scanning electron microscopy (Konerding *et al.*, 2012); that is, subpleural regions of the cardiac lobe demonstrating signficant sprouting and intussusceptive angiogenesis.

To obtain a comparative measure of deformation, transept regions of interest (ROI) were drawn across the planar sections of the cardiac lobe (Figure 7). In general, the displacement of the subpleural regions exceeded, by more than 2-fold, the displacement of the central regions of the lung. Heterogeneity was also noted within these subpleural regions. In general, subpleural regions with significant positive (Figure 7, point 'A') and negative (Figure 7, point 'E') curvature appeared to have greater displacement than regions with less curvature. As noted previously, the posterior aspect of the cardiac lobe had the greatest deformation with approximately 2-fold increase over the corresponding region on the anterior surface of the cardiac lobe (Figure 7, D–E).

5. Discussion

In this report, we used microCT imaging to develop finite element models of the pre- and post-pneumonectomy murine lung. In particular, geometric models of the cardiac lobe demonstrated significant displacement and deformation within the 24 hours after surgery. 2D "maps" of the cardiac lobe deformation were strikingly similar to regions of growth previously documented by histology and imaging studies (Konerding *et al.*, 2012); that is, both deformation and growth occurred in sublpleural regions of the cardiac lobe. The spatial coincidence of parenchymal deformation and lung growth suggests a mechanical signal for triggering lung regeneration.

The principal finding of this report is that there was significant displacement and deformation in the cardiac lobe after pneumonectomy (Figures 3–7). Previous postoperative microCT scanning has indicated a 5 mm shift of the cardiac lobe into the left hemithorax (Gibney *et al.*, 2012); here, we demonstrate that the cardiac lobe also demonstrated marked shape change within 24 hours of pneumonectomy. Since the shape changes occurred within 24 hours—prior to any change in the material composition of the lung (Lin *et al.*, 2011)—the deformation appeared to be the result of transpleural pressure dynamics and not true lung growth.

Located in the inferior mediastinum, the cardiac lobe (also referred to as the infracardiac, postcaval, median and inferior lobe lobe) abuts the preoperative left lung and is contiguous with the post-pneumonectomy pleural space. We speculate that pneumonectomy leads to preferential stretch of the portion of the lung exposed to the pneumonectomy space. With continued diaphragmatic function bilaterally, the cardiac lobe experiences higher levels of cyclic stretch during breathing than more remote regions of the lung. We hypothesize that cyclic stretch, reminiscent of the role of stretch in lung development (Brody & Thurlbeck, 1986) and post-pneumonectomy humans (Butler *et al.*, 2012), may be an important trigger for new lung growth.

The spatial scale of the cardiac lobe deformation reflected the scale of angiogenic growth previously observed in vivo (Konerding *et al.*, 2012). Also consistent with in vivo findings (Konerding *et al.*, 2012), our finite element model demonstrated significant variability in the degree of subpleural deformation. Similarly, our previous analysis of the post-pneumonectomy cardiac lobe has demonstrated discontinuous subpleural regions of angiogenic growth (Konerding *et al.*, 2012). The integral scale of these regions of in vivo growth is strikingly similar to the areas of deformation described in our finite element model. We anticipate that a biologic test of our computational predictions could be obtained by spatial sampling techniques such as laser capture microdissection (LCM). We are

currently using LCM to evaluate the angiogenesis-related transcriptional activity in the subpleural cardiac lobe.

A potential limitation of our study is that the lung deformation calculations were based on static lung images obtained at mid-thoracic volumes (20 cmH_2O). Whereas this shape change reflected one aspect of deformation, a secondary consideration was the potential shape change associated with the dynamics of breathing. With each tidal breath, there is a change in lung volume. Whether this "cyclic" stretch participates in shape change, much less a "stretch" signal for lung growth is unclear. The development of respiratory-gated CT scanning should facilitate the analysis of potential shape change during the breathing cycle.

6. Conclusions

The change in the lung shape after pneumonectomy has been temporally associated with significant compensatory growth of the remaining lung (Hsia *et al.*, 2004). In this report, we used microCT imaging and finite element modeling of the remaining lung after left pneumonectomy to demonstrate significant change in the shape of the cardiac lobe. Deformation of the cardiac lobe was heterogeneous, but concentrated in the subpleural regions of the lobe. We speculate that parenchymal deformation is an important trigger for regenerative lung growth.

Acknowledgments

Supported in part by NIH Grant HL94567, HL75426 and HL07734

Abbreviations

2D	2-dimensional
3D	3-dimensional
LCM	laser capture microdissection
ROI	Region of interest
RDI	relative deformation index

References

Al-Mayah A, Moseley J, Brock KK. Contact surface and material nonlinearity modeling of human lungs. Phys. Med. Biol. 2008; 53:305–317. [PubMed: 18182705]

Brody, JS.; Thurlbeck, WM. Handbook of physiology. The respiratory system. Mechanics of breathing. Vol. vol. 3. Bethesda: Am. Physiol. Soc.; 1986. Development, growth, and aging of the lung; p. 355-386.

Butler J, Loring SH, Patz S, Tsuda A, Yablonskiy DA, Mentzer SJ. Evidence for lung growth in adult humans. N. Engl. J. Med. 2012; 367:244–247. [PubMed: 22808959]

Chamoto K, Gibney BC, Lee GS, Lin M, Simpson DC, Voswinckel R, Konerding MA, Tsuda A, Mentzer SJ. Cd34+ progenitor to endothelial cell transition in post-pneumonectomy angiogenesis. Am. J. Resp. Cell Mol. Biol. 2012 In press.

Eringen, AC. Nonlinear theory of continuous media. New York: McGraw-Hill; 1962.

Gibney B, Houdek J, Lee GS, Ackermann M, Lin M, Simpson DC, Chamoto K, Konerding MA, Tsuda A, Mentzer SJ. Mechanostructural adaptations preceding post-pneumonectomy lung growth. Exp. Lung Res. 2012 In press.

Gibney B, Lee GS, Houdek J, Lin M, Chamoto K, Konerding MA, Tsuda A, Mentzer SJ. Dynamic determination of oxygenation and lung compliance in murine pneumonectomy. Exp. Lung Res. 2011; 37:301–309. [PubMed: 21574875]

Hoffmann CM, Rossignac JR. A road map to solid modeling. IEEE Trans. Vis. Comput. Graphics. 1996; 2:3–10.

Hsia CCW, Berberich MA, Driscoll B, Laubach VE, Lillehei CW, Massaro C, Perkett EA, Pierce RA, Rannels DE, Ryan RM, Tepper RS, Townsley MI, Veness-Meehan KA, Wang N, Warburton D. Mechanisms and limits of induced postnatal lung growth. Am. J. Respir. Crit. Care. Med. 2004; 170:319–343. [PubMed: 15280177]

Kojic, M.; Filipovic, NBSNK. Computer modeling in bioengineering: Theoretical background, examples and software. Chichester, England: John Wiley and Sons; 2008.

Konerding MA, Gibney BC, Houdek J, Chamoto K, Ackermann M, Lee G, Lin M, Tsuda A, Mentzer SJ. Spatial dependence of alveolar angiogenesis in post-pneumonectomy lung growth. Angiogenesis. 2012; 15:23–32. [PubMed: 21969134]

Lin M, Chamoto K, Gibney B, Lee GS, Collings-Simpson D, Houdek J, Konerding MA, Tsuda A, Mentzer SJ. Angiogenesis gene expression in murine endothelial cells during post-pneumonectomy lung growth. Resp. Res. 2011; 12:98.

Malvern, LE. Introduction to the mechanics of continuous medium. Englewood Cliffs, NJ: Prentice-Hall; 1969.

Miki H, Butler JP, Rogers RA, Lehr JL. Geometric hysteresis in pulmonary surface-to-volume ratio during tidal breathing. J. Appl. Physiol. 1993; 75:1630–1636. [PubMed: 8282613]

Milasinovic DZ, Ivanovic MR, Filipovic ND, Kojic MR. Software tools for automatic generation of finite element mesh and application of biomechanical calculation in medicine. Hem. Ind. 2008; 62:177–180.

Tsuda A, Filipovic N, Haberthur D, Dickie R, Matsui Y, Stampanoni M, Schittny JC. Finite element 3d reconstruction of the pulmonary acinus imaged by synchrotron x-ray tomography. J. Appl. Physiol. 2008; 105:964–976. [PubMed: 18583378]

Werner R, Ehrhardt J, Schmidt R, Handels H. Patient-specific finite element modeling of respiratory lung motion using 4d ct image data. Med. Phys. 2009; 36:1500–1511. [PubMed: 19544766]

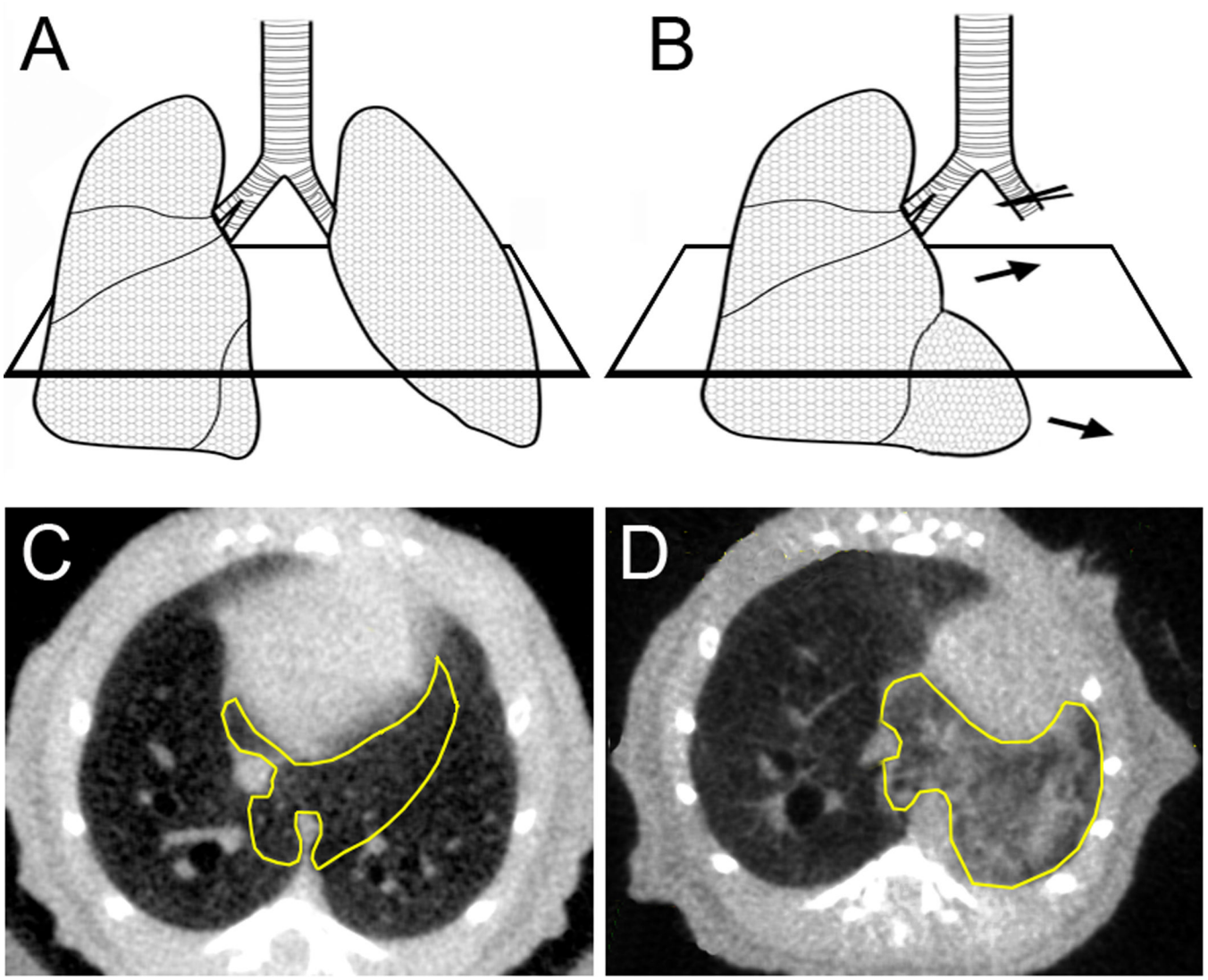

Figure 1.
Schematic and transverse CT scan of the lung before (A,C) and 24 hours after (B,D) pneumonectomy. The cardiac lobe (yellow outline) demonstrates significant shape change within 24 hours.

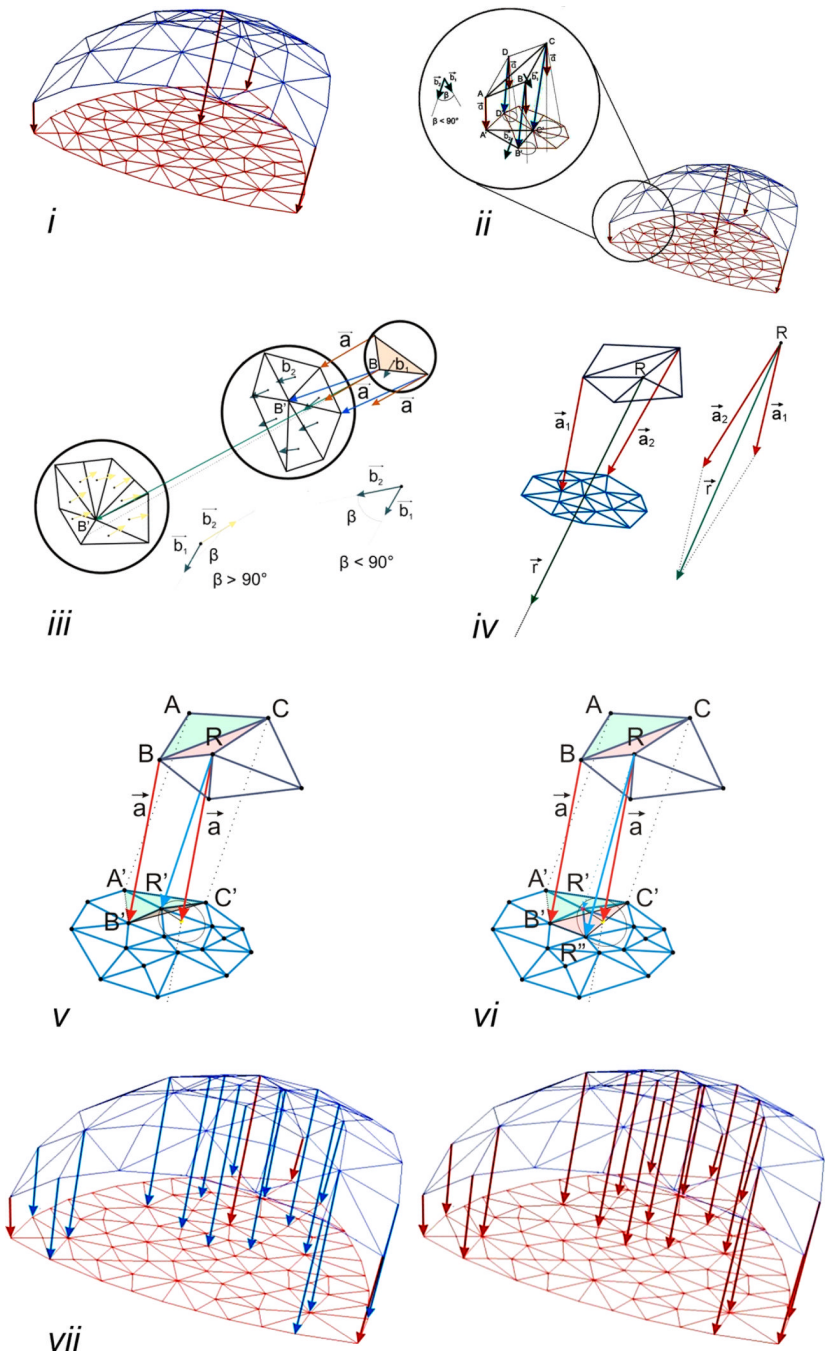

Figure 2.

The registration of pre- and post-pneumonectomy lung images was performed using a nonrigid iterative algorithm. Landmarks and surface features were used to identify initial "key" connections between the corresponding nodes in the pre- and post-pneumonectomy geometric models (i). The manually selected key nodes (Figure 2i, red arrows) provided structural correspondence that was interpolated by the subsequent automated steps of the algorithm (ii-vi). With successive iterations, the number of key nodes increased until all nodes in the pre-pneumonectomy mesh were assigned.

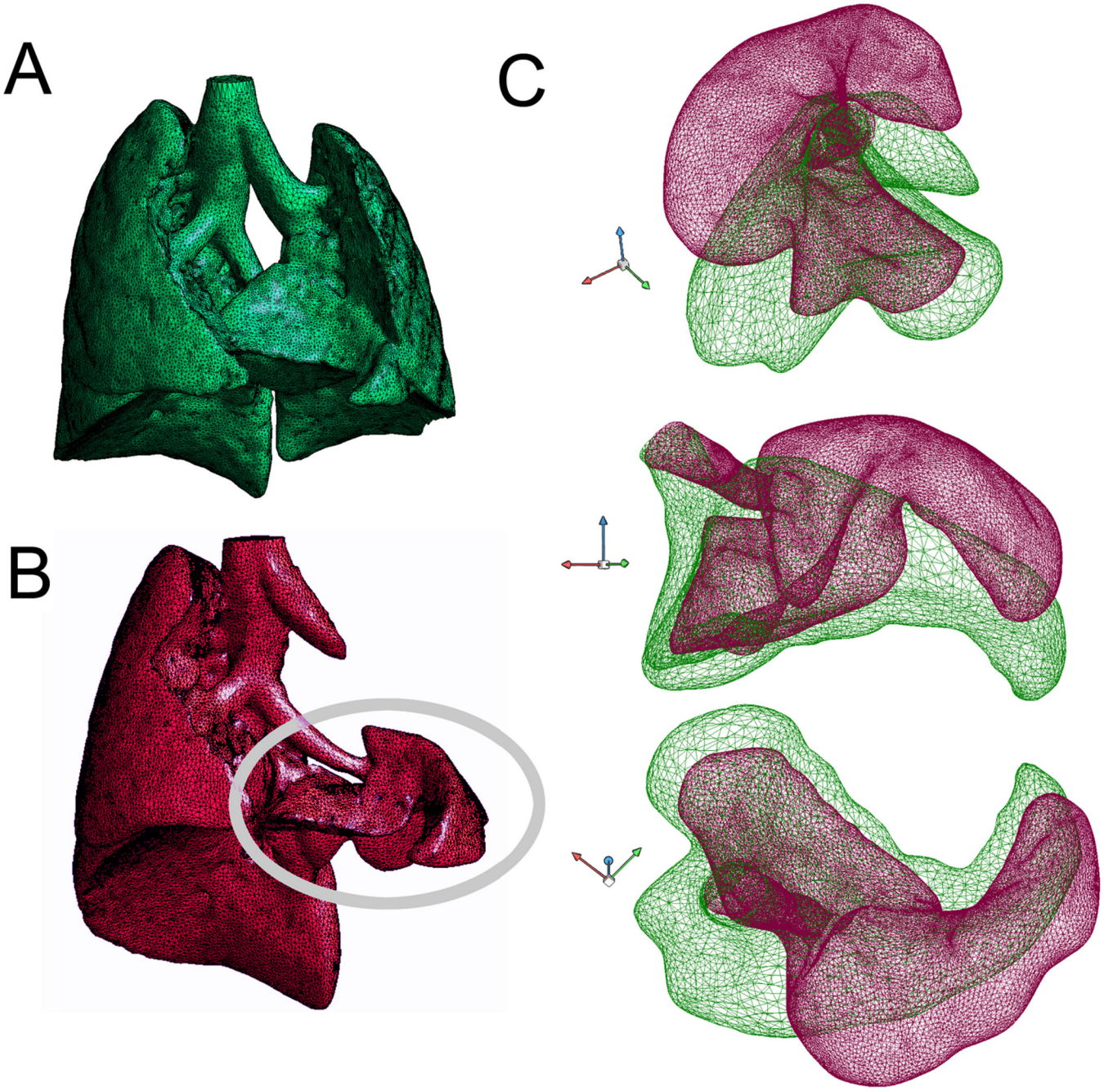

Figure 3.
Geometric models of both lungs before (A) and the remaining right lung 24 hours after (B) pneumonectomy. C) Geometric models of the cardiac lobe (B, elipse) before (green) and after (red) pneumonectomy were superimposed and presented in 3 projections (superior, anterior, inferior). The cardiac lobe airway was used as a reference point for translation and reference axis for rotation.

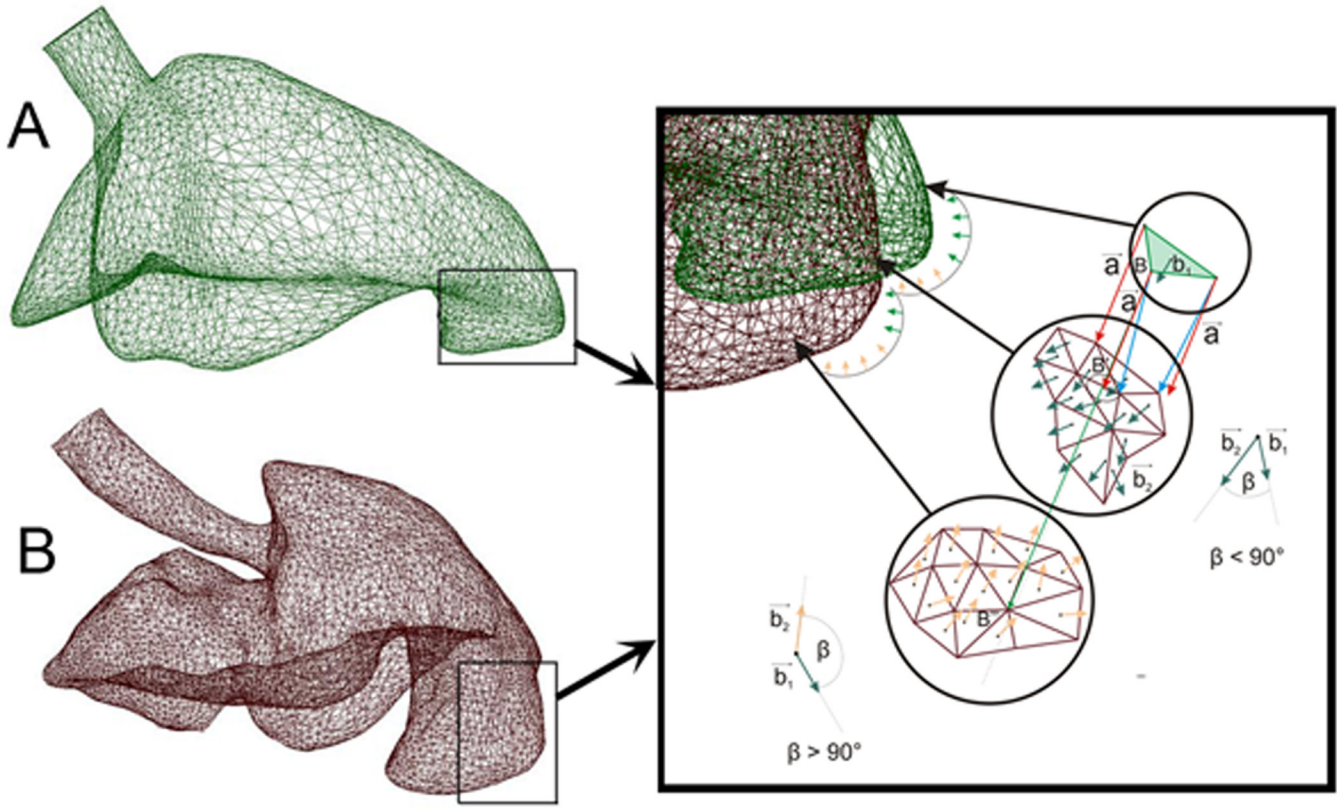

Figure 4.
Structural correspondance of surface features of the pre-pneumonectomy (A) and post-pneumonectomy (B) finite element model. Inset shows the implementation of step 2d (see 3. Numerical Method); the procedure to ensure the proper orientation of the surface elements.

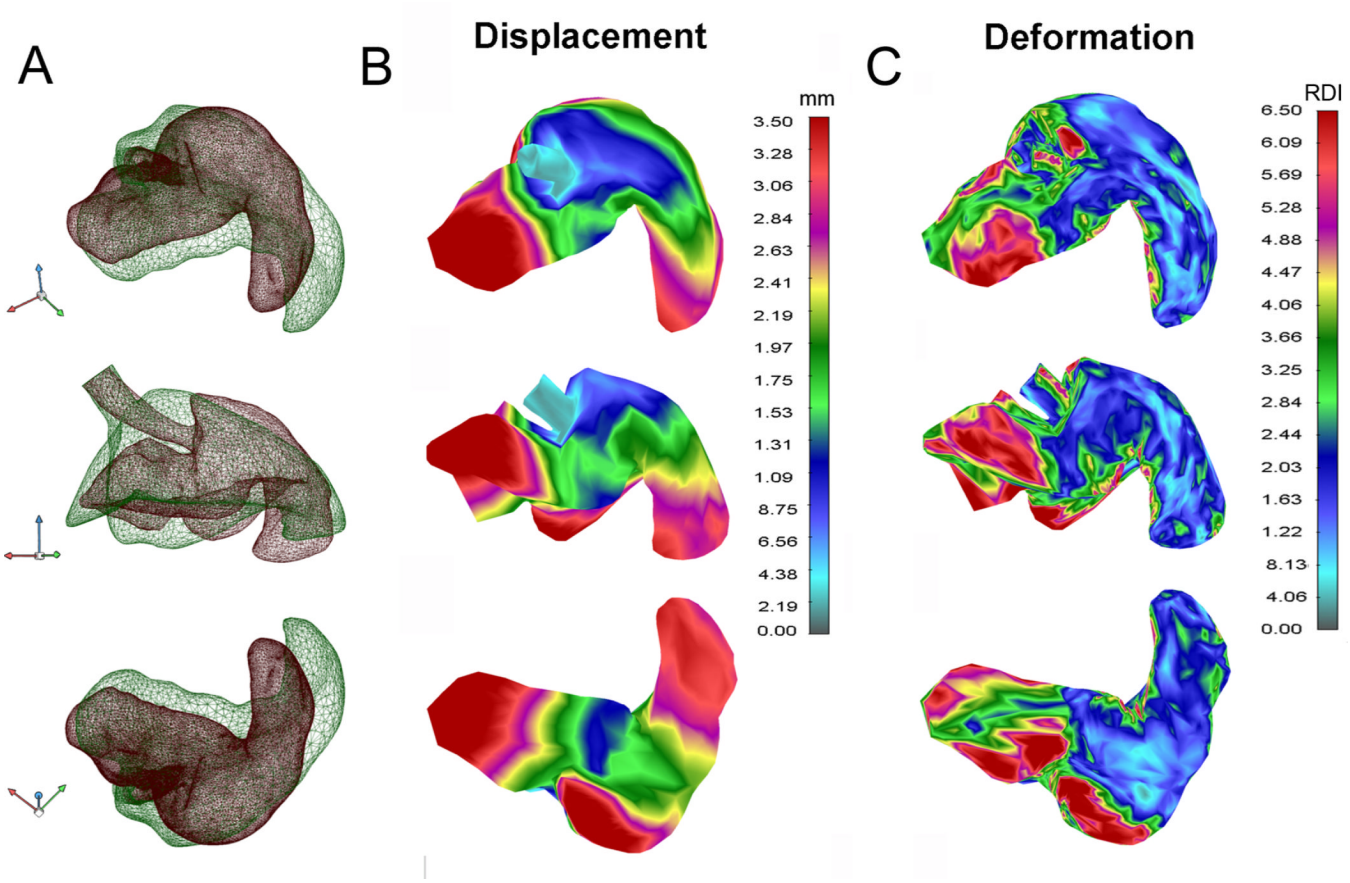

Figure 5.

Displacement and deformation of the cardiac lobe after calculating relative displacement of pre-pneumonectomy and post-pneumonectomy models of the cardiac lobe. A) The superimposed pre- (green) and post-pneumonectomy (red) models were used to calculate displacement (B) and parenchymal deformation (C).

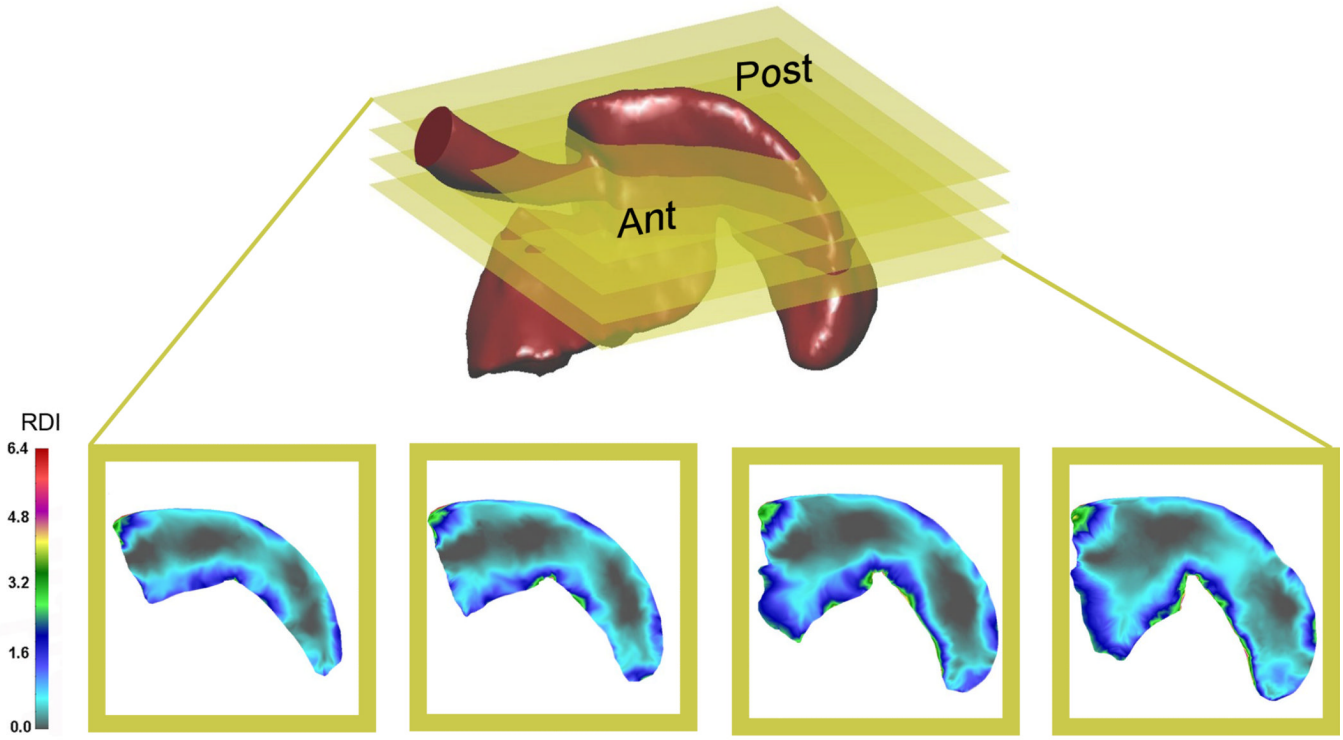

Figure 6.
Transverse sections of the cardiac lobe, analogous to histologic sections, were defined for four distinct planes in the lobe. Total deformation, reflecting the product of stretch and rotation, was mapped to the 2D sections. Ant=anterior or ventral surface; Post= posterior or dorsal surface.

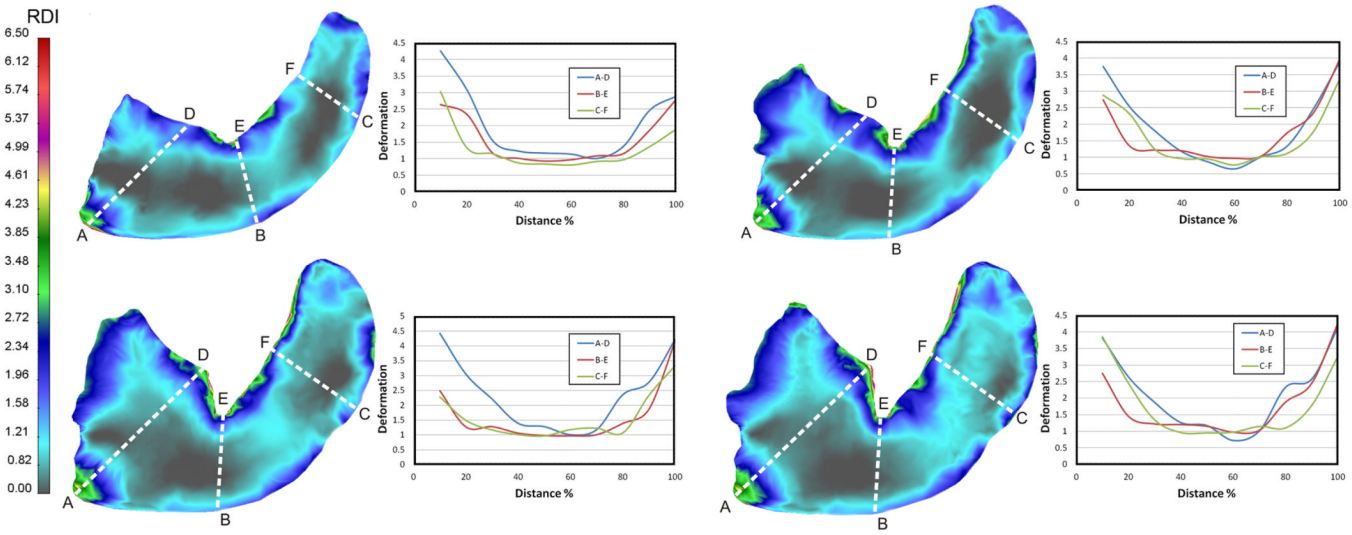

Figure 7.

Quantitative deformation of the cardiac lobe measured in four transverse planes. Transept regions of interest (ROI) drawn across the lobar section in three orientations (A–D, B–E, and C–F). The relative deformation, plotted as a function of distance, is shown in the adjacent graph. Deformation in the subpleural regions was consistently greater than in the center of the cardiac lobe. The posterior aspect of the cardiac lobe is defined by A-B-C; the anterior aspect by D-E-F.